Research Article | Vol. 31, No. 9 / 24 Apr 2023 / Optics Express 13683

Optics EXPRESS

Gouy phase of Bessel-Gaussian beams: theory vs. experiment

LYUBOMIR STOYANOV,[1,2] ALEKSANDER STEFANOV,[3,4] ALEXANDER DREISCHUH,[2,*] AND GERHARD G. PAULUS[1,5]

[1] Institute of Optics and Quantum Electronics, Friedrich Schiller University, Max-Wien-Platz 1, D-07743 Jena, Germany
[2] Department of Quantum Electronics, Faculty of Physics, Sofia University, 5, J. Bourchier Blvd., Sofia-1164, Bulgaria
[3] Department of Mechatronics, Robotics and Mechanics, Faculty of Mathematics and Informatics, Sofia University, 3, J. Bourchier Blvd., Sofia 1164, Bulgaria
[4] Institute of Mathematics and Informatics, Bulgarian Academy of Sciences, Acad. Georgi Bonchev Str., Block 8, Sofia 1113, Bulgaria
[5] Helmholtz Institute Jena, Fröbeltstieg 3, D-07743 Jena, Germany
[*] ald@phys.uni-sofia.bg

Abstract: It is well-known that the wave of a freely propagating Gaussian beam experiences an additional π phase shift compared to a plane wave. This phase shift, known as the Gouy phase, has significant consequences in, e.g., nonlinear optics, since the nonlinear processes require high peak intensity and phase matching of the focused beams. Hence, determining and controlling the Gouy phase is crucial in many fields of modern optics and photonics. Here, we develop an analytical model for the Gouy phase of long-range Bessel-Gaussian beams obtained by annihilating highly charged optical vortices. The model accounts for the influence of the relevant experimental parameters (topological charge, radius-to-width ratio of the initial ring-shaped beam, and focal length of the Fourier-transforming lens). We find an evolution of the Gouy phase varying nearly linearly with propagation distance and confirm this result experimentally.

1. Introduction

One of the phenomena that is assumed to be well understood, but still provokes serious scientific interest, is that any focused light beam experiences an axial phase shift with respect to a reference plane wave when passing through its focus. This phase anomaly was first studied by Gouy and is named after him. The chronology of early studies can be read in the work of Linfoot and Wolf [1]. Later, most of the studies were related to the development of microwave optics (see e.g. [2,3]), lasers (see e.g. [4]), nonlinear optics [5], terahertz radiation [6,7], and singular optics of phase [8,9] and polarization vortices [10,11], including hybrid singularities [12]. The Gouy phase has important consequences in, e.g., nonlinear optics. In general, the n-th order nonlinear polarization will experience a phase shift that is n times larger than that experienced by the incident pump wave [13,14]. As a consequence, the efficiency of third-harmonic generation in the tight-focusing limit, for example, vanishes for the case of perfect phase matching. It can be optimized by introducing a linear wave vector mismatch for compensating the Gouy phase shift [13]. Conversion between Laguerre-Gaussian modes via four-wave mixing in the thick-medium regime (in essence the transfer between azimuthal and radial mode indices) is also observed and explained by the influence of the Gouy phase [15]. It is natural to expect that the Gouy phase also has profound consequences in highly nonlinear processes like above-threshold ionization [16] and high-harmonic generation [17].

Let us denote by L_D and z the Rayleigh diffraction length and the longitudinal coordinate, respectively. Then, the Gouy phase for a fundamental Gaussian beam is given by Φ_G=atan(z/L_D).

#480761
Journal © 2023

https://doi.org/10.1364/OE.480761
Received 11 Nov 2022; revised 19 Jan 2023; accepted 5 Mar 2023; published 11 Apr 2023

Optics EXPRESS

For a higher-order Hermite-Gaussian mode with mode indices (n, m) this phase is multiplied by a factor of $(1+m+n)$ [18]. For a higher-order Laguerre-Gaussian modes with mode indices (ℓ, p) the factor is $(1+|\ell|+2p)$ [19,20]. Here, the modulus accounts for the fact that the azimuthal mode index ℓ (i.e. the on-axis topological charge (TC) of the point-phase dislocation known as optical vortex (OV)) can either be positive or negative. The factor 2 is related to the fact that p is the radial mode index of the LG beam. Generally speaking, passing through the focal plane, higher-order Hermite-Gaussian and Laguerre-Gaussian modes accumulate a higher Gouy phase with respect to a reference Gaussian beam. This has been proven experimentally for truncated Gaussian beams as well [21].

The question we would like to address in this communication is how the Gouy phase behaves in Bessel-Gaussian beams. Bessel beams are one of the four types of exact solutions of the Helmholtz equation [22]. For instance, in the pure mathematical sense, the zeroth order Bessel beam has a sharp central non-diffracting peak surrounded by an infinite number of satellite rings that are offset by π in phase with respect to their neighbor. An infinite number of surrounding rings implies infinite energy, which obviously is not possible for (Gaussian) laser beams with finite transverse dimensions. Viable approximations to Bessel beams have a Gaussian envelope and are usually denoted as Bessel-Gaussian beams (BGBs). Their central peaks (for higher order BGBs: rings) are remarkably resistant against diffraction. Therefore, BGBs are sometimes denoted as "non-diffracting", "quasi-non-diffracting" or "diffraction-free" in the literature [23–25].

Well-known methods for generating BGBs are annular slits in the back focal plane of a lens [23,24,26] or even a cylindrical lens morphed to a closed ring [27]. Other methods use axicons [26], or deformable mirrors [28], or spatial light modulators reproducing the phase structures of reflective axicons [29], or computer-generated holograms of axicons [30]. In previous studies, we have demonstrated the possibility to generate long-range BGBs by creating and annihilating highly charged optical vortices [31,32]. The method was demonstrated to work even for sub-7-femtosecond pulses [33].

Due to the extended interaction length of the Bessel-Gaussian beams, they find application in many fields of physics, e.g. in plasma physics [34,35] and in strong-field physics [17,36]. An interesting application of BGBs benefiting from their extended range of strong focusing might be high-harmonic generation (HHG) [37,38]. Then, immediate question concerns the Gouy phase in long-range BGBs because of its impact on phase matching of high harmonics.

The Gouy phase is quantified on the axis of a real beam relative to a reference infinite plane wave, which, since not spatially confined, does not diffract. The central peaks of Bessel-Gaussian beams (BGBs) have remarkably low divergences on the order of microradians [27,31]. Therefore, one might guess that BGBs have negligible Gouy phase. However, the two experimental works we are aware of [8,39] found that for strong focusing the Gouy phase of BGBs changes linearly for propagation distances of fractions of millimeters (up to 5π within 1 mm [8] and up to 6π within 6 µm [39]).

In this work we develop an analytical model for the Gouy phase of long-range BGBs that accounts for the relevant experimental parameters. The analytical results are found to be in good quantitative agreement with the experimental data. In particular, under relatively weak focusing of the initial hollow ring-shaped beam (lens' focal lengths 40-75 cm), the Gouy phase of the BGB is found to change nearly linearly at a rate of some $0.15\,\pi$/cm over a distance of 45 cm. Under moderate focusing (with a lens focal length ~15 cm), the linear vs. propagation distance Gouy phase reaches a slope of $1.0\,\pi$/mm over distances exceeding 4 mm. The reported data could appear important for the phase matching in the process of high-harmonics generation [40] when using BGBs as opposed to conventional Gaussian beams (see e.g. [37,38]).

Optics EXPRESS

2. Theoretical model

2.1. Elementary theory

We start with the insight that the wave vectors $\vec{k}$ of confined beams necessarily have a transverse component k_t. Since $k^2 = k_t^2 + k_z^2$, where k_z is the longitudinal component of the wavenumber k, this means that a finite transversal wave number k_t goes at the expense of k_z: The narrower the BGB, the larger k_t and the smaller k_z. This results in an effectively increasing wavelength (or a phase advancing faster than the speed of light), which can be seen as the physical origin of the Gouy phase.

The accumulated phase difference $\Delta\phi$ between a Bessel beam and a plane wave is

$$\Delta\phi = \Delta kz = (k - k_z)z, \tag{1}$$

where z is distance along the optical axis. Then the distance $\mathcal{D}$ for a phase difference of 2π is

$$\mathcal{D} = \frac{2\pi}{k - k_z}. \tag{2}$$

In order to estimate transversal wave number k_t, we note that the first zero of $J_0(x)$ is at $x = 2.4048\cdots$. Therefore, when ρ is the radius of the central peak of the Bessel beam, k_t can be estimated as

$$k_t\rho = 2.4048 \qquad \text{or} \qquad k_t = 2\pi\frac{0.38274}{\rho}. \tag{3}$$

Using the approximation $k_z = \sqrt{k^2 - k_t^2} \approx k - \frac{k_t^2}{2k}$, i.e. limiting the Taylor expansion at $k = 0$ to second order ($k_t \ll k$), we get

$$k_z \approx k - \frac{(2\pi \times 0.38274/\rho)^2}{2k} \tag{4}$$

which, along with Eq. (2) and the fact that $k = \frac{2\pi}{\lambda}$ implies that

$$\mathcal{D} = 13.65\frac{\rho^2}{\lambda}. \tag{5}$$

2.2. Derivation of the Fourier transform leading to Bessel-Gaussian beams

Let $\mathcal{F}\{U\}$ denote the Fourier transform of a function $U(x, y)$ and $\mathcal{H}_\ell\{U(r)\}$ stand for the Hankel transform of order ℓ of a radially symmetric function. The Fourier conjugate variables corresponding to Cartesian coordinates (x, y) and polar coordinates (r, θ) will be denoted by (u, v) and (ρ, φ), respectively. We will also denote the Fourier transform of $U(r, \theta)$ as $U(\rho, \varphi)$ where convenient and where the context is unambiguous.

Let us consider $U(r, \theta)$ as a function separable in polar coordinates, i.e. $U(r, \theta) = R(r)F(\theta)$. Then one can do the following expansion [41]

$$\mathcal{F}\{U(r, \theta)\} = \sum_{n=-\infty}^{\infty} c_n(-i)^n \exp(in\varphi)\mathcal{H}_\ell\{R(r)\} \tag{6}$$

with coefficients c_n given by

$$c_n = \frac{1}{2\pi}\int_0^{2\pi} F(\theta)\exp(-in\theta)d\theta. \tag{7}$$

When $F(\theta) = \exp(i\ell\theta)$ we get $c_n = \delta_{n\ell}$, where $\delta_{n\ell}$ is the Kronecker delta. For the Fourier transform this results in

$$\mathcal{F}\{U(r,\theta)\} = (-i)^{\ell} \exp(i\ell\varphi)\mathcal{H}_\ell\{R(r)\}. \tag{8}$$

Applying the Fourier transform twice we get

$$\mathcal{F}^2\{U(r,\theta)\} = (-i)^{2\ell} \exp(i\ell\theta)\mathcal{H}_\ell^2\{R(r)\} = (-1)^{\ell} U(r,\theta), \tag{9}$$

since the Hankel transform is its own inverse.

Another important identity that we need is [42]

$$\begin{aligned}\exp\left(-\frac{r^2+r_0^2}{\omega_0^2}\right) I_\ell\left(\frac{2rr_0}{\omega_0^2}\right) &= \frac{\omega_0^2}{2}\int_0^\infty \exp\left(-\frac{\omega_0^2\rho^2}{4}\right) J_\ell(r_0\rho)J_\ell(r\rho)\rho d\rho \\ &= \frac{\omega_0^2}{2}\mathcal{H}_\ell\left\{\exp\left(-\frac{\omega_0^2\rho^2}{4}\right) J_\ell(r_0\rho)\right\}.\end{aligned} \tag{10}$$

Here I_ℓ is the modified Bessel function of the first kind and J_ℓ denotes the Bessel function, both of order ℓ.

Let

$$E(r,\theta) = \exp(i\ell\theta)\exp\left(-\frac{(r-r_0)^2}{\omega_0^2}\right), \tag{11}$$

where ω_0 and r_0 are positive real parameters. The physical meaning of Eq. (11) is the description of the electric field amplitude E of a bright ring-shaped beam with radius r_0 and ring width ω_0 (panel (a) of Fig. 1). It is a very good approximation for an optical vortex with a topological charge ℓ (ℓ is an integer number). The phase distribution for $\ell = +1$ and $\ell = -9$ is displayed in Fig. 1, panels (b) and (c).

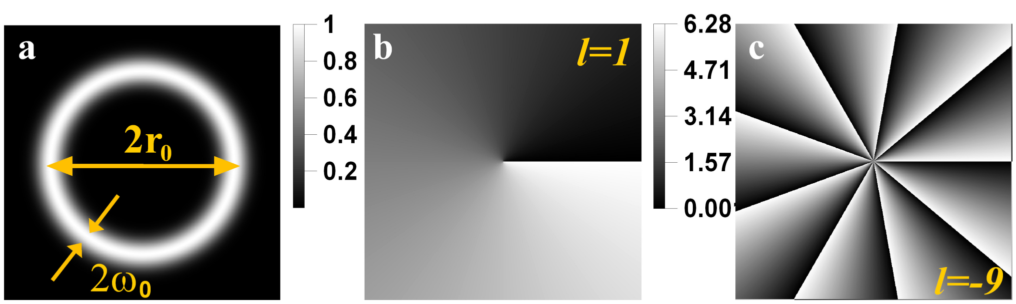

Fig. 1. (a) Illustration of an optical field amplitude as defined by Eq. (11) with $r_0 = 0.5$ and $w_0 = 0.075$ in arbitrary units. (b) and (c) spiral phase distributions of optical vortices with topological charges (TCs) $\ell = 1$ and $\ell = -9$, respectively. The opposite signs of the TCs can easily be recognized by the opposite phase gradients, while their magnitudes can be determining by counting the azimuthal 2π-periods presented in grayscale.

By expanding the square we get

$$E(r,\theta) = \exp(i\ell\theta)\exp\left(-\frac{r^2+r_0^2}{\omega_0^2}\right)\exp\left(\frac{2rr_0}{\omega_0^2}\right). \tag{12}$$

Then, for large r_0, the last exponent can be viewed as an approximation of the modified Bessel function of the first kind

$$\exp\left(\frac{2rr_0}{\omega_0^2}\right) \approx I_\ell\left(\frac{2rr_0}{\omega_0^2}\right), \tag{13}$$

Optics EXPRESS

which means that the electric field amplitude can be written as

$$E(r,\theta)=\exp(i\ell\theta)\exp\left(-\frac{r^2+r_0^2}{\omega_0^2}\right)I_\ell\left(\frac{2rr_0}{\omega_0^2}\right). \tag{14}$$

From the above and considering Eqs. (8) and (10) we get

$$\begin{aligned}E(r,\theta)&=\exp(i\ell\theta)\frac{\omega_0^2}{2}\mathcal{H}_\ell\left\{\exp\left(-\frac{\omega_0^2\rho^2}{4}\right)J_\ell(r_0\rho)\right\}\\&=\frac{\omega_0^2}{2(-i)^\ell}\mathcal{F}\left\{\exp(i\ell\varphi)\exp\left(-\frac{\omega_0^2\rho^2}{4}\right)J_\ell(r_0\rho)\right\}.\end{aligned} \tag{15}$$

By taking the Fourier transform again and using Eq. (9), we get

$$\begin{aligned}\mathcal{F}\{E(r,\theta)\}&=\frac{\omega_0^2(-i)^\ell}{2}\exp(i\ell\varphi)\exp\left(-\frac{\omega_0^2\rho^2}{4}\right)J_\ell(r_0\rho),\\E(\rho,\varphi)&=\frac{\omega_0^2}{2}\exp\left(i\ell\varphi-\frac{i\ell\pi}{2}\right)\exp\left(-\frac{\omega_0^2\rho^2}{4}\right)J_\ell(r_0\rho).\end{aligned} \tag{16}$$

This, in essence, is the final result derived in [31], meaning that the Fourier transform of a thin bright ring is, to a good approximation, a Bessel-Gaussian beam (BGB). For $\ell=0$, i.e. a flat phase front of the bright ring-shaped beam in front of the focusing (i.e. Fourier-transforming) lens, the result is a zeroth-order BGB (panels (a1) and (a2) of Fig. 2) and for $|\ell|>0$ an ℓ-th order BGB (see panels (b1) and (b2) for $|\ell|=1$).

2.3. Gouy phase of a BGB obtained by direct comparison with a plane wave

Let us consider the general Bessel-Gaussian solution of the scalar Helmholtz equation, given by Gori et al. [43]

$$V(\rho,z)=A\frac{\omega_0}{\omega(z)}e^{i(k-\frac{\beta^2}{2k})z-i\Phi(z)}J_0\left(\frac{\beta\rho}{(1+i\frac{z}{L})}\right)\exp\left[\left(-\frac{1}{\omega^2(z)}+\frac{ik}{2R(z)}\right)\left(\rho^2+\frac{\beta^2z^2}{k^2}\right)\right]. \tag{17}$$

Here, V is the electric field amplitude, ρ is the radial coordinate and z stands for the longitudinal coordinate along which the beam (ring width ω_0, radius of curvature of the phase front $R(z)$, and phase term $\Phi(z)$) evolves. k is the wavenumber, β is related to the width of the central peak of the BGB, $L=k\omega_0^2/2$, and

$$\omega(z)=\omega_0\sqrt{1+\frac{z}{L}^2},\quad \Phi(z)=\arctan\left(\frac{z}{L}\right),\quad R(z)=z+\frac{L^2}{z}=\frac{z^2+L^2}{z}. \tag{18}$$

The Gouy phase can be found by direct comparison with the phase of a plane wave at the beam axis ($\rho=0$), (for example see the article by Martelli et al. [25])

$$\Phi_G=-i\,\mathrm{Log}\left(e^{-izk}\lim_{\rho\to0}\frac{V(\rho,z)}{|V(\rho,z)|}\right)=-i\,\mathrm{Log}(e^{-izk}F(z)), \tag{19}$$

where

$$F(z)=\lim_{\rho\to0}\frac{V(\rho,z)}{|V(\rho,z)|}. \tag{20}$$

By Log we denote the principal value of the complex logarithm. The above equation uses the fact that dividing any complex number by its absolute value leaves only the phase factor. Then

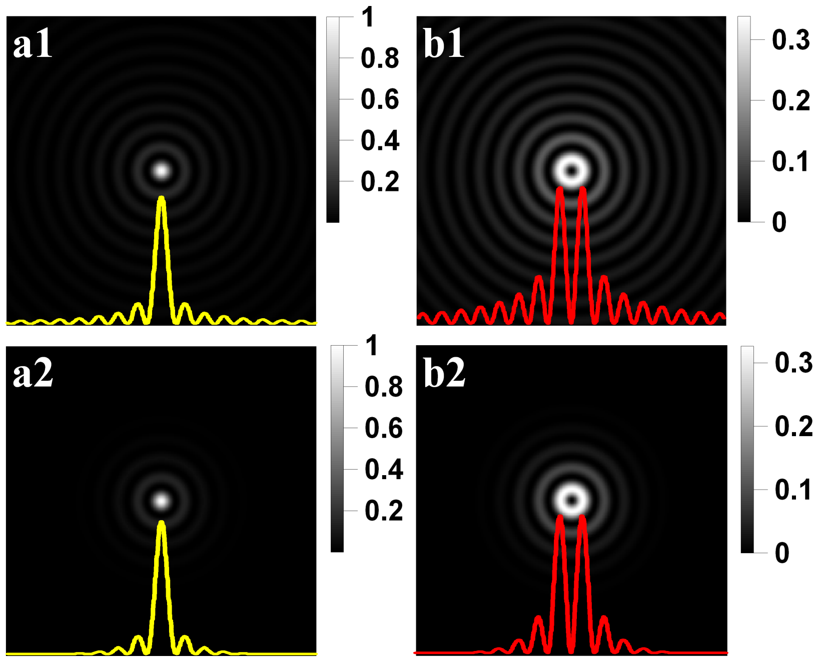

Fig. 2. Intensity distributions of pure zeroth- (a1) and first-order Bessel beams (b1) for $r_0 = 0.5$ arb. units. Corresponding Bessel-Gaussian beams (a2) and (b2) obtained by multiplying the Bessel beams by Gaussian envelopes with $w_0 = 0.075$ arb. units (see Eq. (16)). Note that the relatively flat central part of the Gaussian envelope only weakly reduces the peak intensities of the BGBs while its rapidly decreasing wings causes the BGBs to carry finite number of surrounding rings.

taking the complex logarithm yields the phase. Now, since $V(\rho, z)$ is continuous at $\rho = 0$ and $V(0, z) \neq 0$, we can write for the limit

$$\lim_{\rho\to 0} \frac{V(\rho, z)}{|V(\rho, z)|} = \frac{V(0, z)}{|V(0, z)|} = \frac{A\frac{\omega_0}{\omega(z)} e^{i(k-\beta^2/2k)z - i\Phi(z)} J_0(0) e^{\left(-\frac{1}{\omega^2(z)} + \frac{ik}{2R(z)}\right)\left(\frac{\beta^2 z^2}{k^2}\right)}}{A\frac{\omega_0}{\omega(z)} \, |J_0(0)| \; e^{\left(-\frac{1}{\omega^2(z)}\right)\left(\frac{\beta^2 z^2}{k^2}\right)}}. \tag{21}$$

Taking into account that $J_0(0) = 1$ and simplifying the above we get

$$F(z) = e^{ikz} e^{-i\beta^2/2kz} e^{-i\Phi(z)} e^{i\frac{\beta^2 z^2}{2kR(z)}}, \tag{22}$$

which means that

$$\Phi_G = -\frac{\beta^2}{2k} z + \frac{\beta^2 z^3}{2k(z^2 + L^2)} - \arctan\left(\frac{z}{L}\right). \tag{23}$$

We will represent the above as a sum of two terms

$$\Phi_G = \psi_1(\beta, k, z) + \psi_2(\beta, k, z, L), \tag{24}$$

where

$$\begin{aligned} \psi_1(\beta, k, z) &= -\frac{\beta^2}{2k} z, \\ \psi_2(\beta, k, z, L) &= \frac{\beta^2 z^3}{2k(z^2 + L^2)} - \arctan\left(\frac{z}{L}\right). \end{aligned} \tag{25}$$

Optics EXPRESS

We interpret the above expression for the Gouy phase Φ_G of a BGB as a sum of the Gouy phase of a pure Bessel beam, ψ_1, and an additional term, ψ_2, resulting from the Gaussian envelope background.

2.4. Effect of the focal length of the lens

A thin lens acts as a Fourier-transforming element (see Section 5.2.2 in [41]). Let f be the focal length of the lens and k the wave number. For an initial electric field amplitude $U(x, y)$, after the lens we have

$$\begin{aligned} U(u,v) &= \frac{\exp\left(i\frac{k}{2f}\left(1-\frac{d}{f}\right)\left(u^2+v^2\right)\right)}{i\lambda f}\mathcal{F}\{U\}\left(\frac{uk}{f},\frac{vk}{f}\right) \\ &= \frac{\exp\left(i\frac{k}{2f}\left(1-\frac{d}{f}\right)\rho^2\right)}{i\lambda f}\sum_{n=-\infty}^{\infty} c_n(-i)^n H_\ell\left\{R(r)\right\}\left(\frac{\rho k}{f}\right), \end{aligned} \tag{26}$$

where d is the distance from the input plane to the focusing lens. Now, let us include the lens parameters in the Fourier transform of Eq. (15). To that end, let us concentrate on the Hankel transform. We have

$$H_\ell\left\{\exp\left(-\frac{\omega^2\rho^2}{4}\right)J_\ell(r_0\rho)\right\}(r) = \int_0^\infty \exp\left(-\frac{\omega_0\rho^2}{4}\right)J_\ell(r_0\rho)J_\ell(r\rho)\rho d\rho. \tag{27}$$

Let us make the substitution $\rho \longrightarrow \frac{k\rho'}{f}$ in the above equation (note that the limits of the integral remain the same). Then

$$\int_0^\infty \exp\left(-\frac{\omega_0\rho^2}{4}\right)J_\ell(r_0\rho)J_\ell(r\rho)\rho d\rho = \frac{k^2}{f^2}\int_0^\infty \exp\left(-\frac{\omega_0 k^2\rho'^2}{4f^2}\right)J_\ell\left(r_0\frac{k}{f}\rho'\right)J_\ell\left(\frac{rk}{f}\rho'\right)\rho' d\rho'$$

which we can use to represent the Hankel transform as

$$H_\ell\left\{\exp\left(-\frac{\omega^2\rho^2}{4}\right)J_\ell(r_0\rho)\right\}(r) = \frac{k^2}{f^2}H_\ell\left\{\exp\left(-\frac{\omega^2k^2\rho'^2}{4f^2}\right)J_\ell\left(r_0\frac{k}{f}\rho'\right)\right\}\left(\frac{rk}{f}\right). \tag{28}$$

Applying the above to our case (i.e. Eq. (16) with lens parameters included) and omitting the primes, we have

$$E(\rho,\varphi) = \frac{\omega_0^2k^2}{f^4}\exp\left(i\ell\left(\varphi-\frac{\pi}{2}\right)\right)\exp\left(-\frac{\omega_0^2k^2\rho^2}{4f^2}\right)J_\ell\left(r_0\frac{k}{f}\rho\right). \tag{29}$$

Eq. (29) describes the field amplitude of a BGB resulting from a thin ($r_0/\omega_0 \gg 1$) bright ring-shaped beam focused by a thin lens. Note that we have ignored the phase factor multiplying the sum in Eq. (26), since it does not affect the Gouy phase. Now, let us consider the BGB given by Eq. (17) at $z = 0$ and the resulting Gouy phase Φ_G:

$$\begin{aligned} V(\rho) &= Ae^{-\frac{\rho^2}{\omega^2}}J_0(\beta\rho), \\ \Phi_G &= -\frac{\beta^2}{2k}z + \frac{\beta^2 z^2}{2kR(z)} - \Phi(z). \end{aligned} \tag{30}$$

Comparing Eq. (29) with Eq. (30) we see that

$$\omega = \frac{2f}{\omega_0 k}, \quad \beta = \frac{r_0 k}{f}, \quad L = \frac{k\omega^2}{2} = \frac{2f^2}{\omega_0^2 k}, \tag{31}$$

which leaves the Gouy phase to be

$$\Phi_G(z) = -\frac{r_0^2 k}{2f^2} z + \frac{r_0^2 k}{2f^2} \frac{z^3}{(z^2 + L^2)} - \arctan\left(\frac{z}{L}\right). \tag{32}$$

The second equation in Eq. (31) clearly indicates that the width of the central peak of the BGB is narrower (β is larger) when the initial radius r_0 of the ring-shaped beam is larger and/or the focal length f of the lens is shorter. With respect to the experiments presented in this work it is worth mentioning that when using OVs for the creation of ring-shaped beams, the higher the TC of the OV, the higher the ratio r_0/ω_0 (Fig. 2(b) in [31]). The above result is in full agreement with what can be derived based on physical intuition and first principles.

Equation (5) clearly shows that the distance to be passed for a 2π phase shift is shorter for BGBs with narrower central peaks, i.e. for BGBs created with lenses of shorter focal lengths and with ring-shaped beams of larger radii. From Eq. (3) we can see that k_t is the coefficient β in Eqs. (17) and (30). Now, let us consider ψ_1 from Eq. (25). (We took the sign to be positive, since it makes no difference.) The distance, needed for a 2π phase shift is

$$\frac{\beta^2}{2k}\mathcal{D} = 2\pi \qquad \text{or} \qquad \mathcal{D} = \frac{4\pi k}{\beta^2}. \tag{33}$$

Taking into account that

$$k = \frac{2\pi}{\lambda}, \quad \beta = \frac{2.4048}{\rho} = 2\pi\frac{0.38274}{\rho}, \tag{34}$$

we get

$$\mathcal{D} = \frac{8\pi^2}{4\pi^2 0.38^2}\frac{\rho^2}{\lambda} = \frac{2\rho^2}{0.38^2\lambda} = 13.65\frac{\rho^2}{\lambda}. \tag{35}$$

So, this result is identical to the result obtained using simple arguments (Eq. (5)) and may appear valuable for preliminary estimations of experimental conditions.

3. Experimental comparison with the theoretical results

3.1. Experimental schemes

For the experiments we used two different arrangements. The setup shown in Fig. 3(a) is used to study the Gouy phase of BGBs under relatively weak focusing (lens' focal lengths 40-75 cm). A continuous-wave beam from a frequency-doubled Neodymium-doped Yttrium Orthovanadate ($Nd:YVO_4$) laser (wavelength of 532 nm) was expanded and split to form an object and a reference arm. Passing through the object arm, it is reflected twice from the liquid-crystal spatial light modulators SLM1 and SLM2 (1920 pix × 1080 pix with a pixel pitch of 8 μm and SLM1-to-SLM2 distance of 49 cm). On SLM1 the phase of the desired highly-charged OV is encoded. During propagation towards SLM2, this OV decays into singly-charged OVs which repel each other and reorder in a ring thus generating a ring-shaped beam (see e.g. panel (a) in Fig. 1). This beam still carries point phase singularities, which need to be removed. Since the SLMs are reflective and reflection inverts the sign of TCs, we encode the phase of the same highly-charged OV on SLM2 for subsequent zeroth-order BGB generation. After all TCs of the OVs are erased, the required hollow ring-shaped beam is Fourier transformed in space. This is done by using thin plano-convex lenses with focal lengths f = 75 cm, 50 cm, and 40 cm and diameters of 2.5 cm. Recorded frames of the ring-shaped beam in front of the Fourier-transforming lens and of the generated BGB at a propagation distance of 40 cm behind the focus are shown in Fig. 3, frames (a2) and (a3) respectively. The object and the reference beams are recombined by a second beam splitter to interfere on a CCD camera's chip. The CCD camera is mounted on a rail to allow recording of interference patterns at varying propagation distances.

Optics EXPRESS

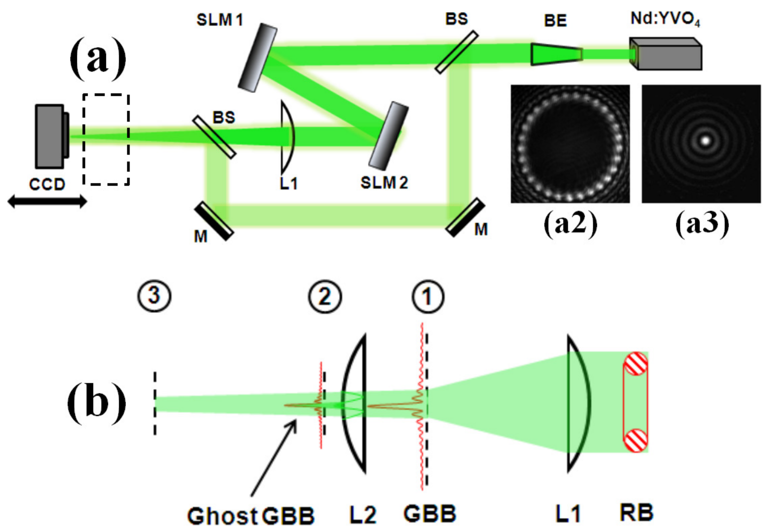

Fig. 3. (a) Setup based on a Mach-Zehnder interferometer. Nd:YVO_4: laser emitting at a wavelength 532 nm, BE: beam expander, BS: beam splitters, M: flat mirrors, SLM: two identical spatial light modulators, L: lens with a focal length of 75 cm, 50 cm, or 40 cm, CCD: charge-coupled device camera placed on a rail to follow the beam behind the focal plane of the lens. Recorded frames of the ring-shaped beam (a2) in front of the Fourier-transforming lens and of the generated BGB (a3) at a propagation distance of 40 cm behind the focus. (b) Single-lens interferometer setup: RB: ring-shaped beam with already erased topological charges of the OVs, L1: focusing lens with $f = 75$ cm forming a Bessel-Gaussian beam in and after its focal plane, L2: focusing lens with $f = 100$ cm forming the "ghost" BGB which is interfering with the central peak of the main BGB. The distance between L1 and L2 is 85 cm.

The setup shown in Fig. 3(b), enabling interferometry for moderate and tight focusing, is a modification to the one shown in Fig. 3(a) in the sense that lens L2 is located approximately at the position of the dashed rectangle in Fig. 3(a). The reference beam is blocked and the second BS removed, while the focusing lens L1 is left unchanged and the CCD camera is relocated close to lens L2. After this modification, lens L1 is still playing the role of the Fourier-transforming element for the ring-shaped beam, thus generating the BGB. The long dash-dotted vertical line (at position 1) is intended to mark the distance at which the main BGB is already well developed. Lens L2 is placed in such a way that it focuses this BGB. It is important to note that in and after the focus of L2 (leftmost dashed vertical line, position 3) the converging BGB is inversely Fourier transformed into a ring-shaped beam. Until then it is propagating as a Bessel-Gaussian beam.

Lens L1 has a focal length of 75 cm, while L2 has 100 cm. In addition, lens L2 has no antireflection coating. Due to this fact, after two weak Fresnel reflections from its surfaces, a "ghost" BGB is formed at a much shorter distance (14.6 cm) than the focal length of L2. This "ghost" BGB is co-axial with respect to the main "background" BGB (see the tiny dark green lines inside lens L2 in Fig. 3(b)). The central peak of the host BGB effectively serves as a reference beam in the very short single-lens interferometer. Within this distance the weakly focused host BGB is only slightly reshaped. A clear interference pattern between the central peak of main BGB and the "ghost" can be observed in a short range of distances near L2. A detailed description of single-lens interferometers can be found in [44,45].

Since the single-lens interferometer is a frugal but not very popular device [45], we demonstrate its use with a Gaussian laser beam in Fig. 4. According to [44] the effective focal length of the

Optics EXPRESS

lens forming the single-lens interferometer is

$$f_{\text{eff}} = \frac{n-1}{3n-1} f, \tag{36}$$

where n is the refractive index of the material and f is the focal length of the lens. For the used N-BK7 lens with $f = 100$ cm the focal plane is estimated to be located 14.6 cm behind the lens. The left two frames in Fig. 4 show interferograms recorded at distances of ±7.5 mm from the focus of the "ghost" beam. Their symmetrical displacement relative to the focus can be recognized by the change in the angle of the moderately pronounced ellipticity of the interference rings. The ellipticity of the Gaussian beam (the ratio of the major to the minor axis of the ellipse) was estimated to be 1.15. Elliptic beam profiles result in different Rayleigh diffraction lengths along the major and the minor axis of the elliptical beam, thus affecting the Gouy phase measurement. The mentioned estimated ellipticity results in a 15 % difference between the Rayleigh diffraction lengths along the two axes (see dashed curves in Fig. 4(c)).

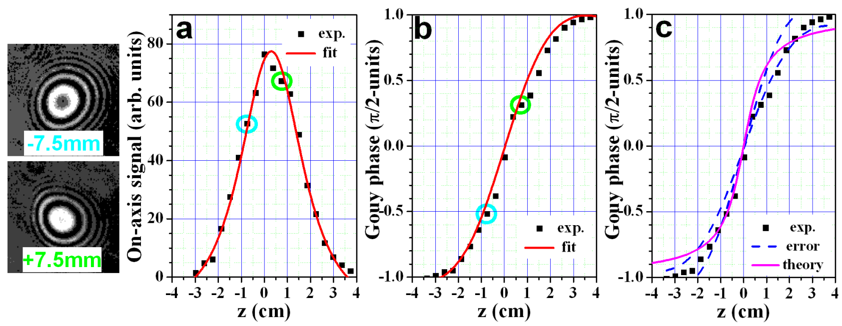

Fig. 4. Test measurements with a Gaussian beam and a single-lens interferometer. Left panels: Interference patterns recorded at ±7.5 mm with respect to the lens' focus. These positions are labelled with colored circles in graph (a) showing the on-axis interference signal vs. distance and on graph (b) presenting the retrieved Gouy phase of the Gaussian beam. Graph (c) – the processed experimental points for the Gouy phase shown already in graph (b), along with two additional dashed curves indicating the uncertainty of the processed data when the ±7.5 % uncertainty of the Rayleigh lengths due to the beam ellipticity is considered. Solid magenta curve – theoretical plot based on the used laser and focusing parameters. See the text for details.

An important fact is the significant change in the interference pattern along the beam axis – from a relatively low on-axis intensity level (due to a destructive interference) before the focus (e.g. at −7.5 mm) towards a global interference maximum at the focus, followed by a decrease of the on-axis interference signal (e.g. at +7.5 mm; although there is an on-axis constructive interference). This is also in agreement with the data in Figs. 4 and 5 in [44]. The graph in Fig. 4(a) shows the essential part of the experimentally recorded on-axis interference signal vs. distance (solid squares; within an interval of 8 cm). Figure 4(b) presents the Gouy phase of the Gaussian beam retrieved from the data in Fig. 4(a), plotted in units of $\pi/2$. The data points denoted with colored circles correspond to the interferograms shown in the left two panels of this figure. The graph in Fig. 4(b) is in a good quantitative agreement with the fact that, along the optical axis around the focus, a freely propagating Gaussian "ghost" beam accumulates a π phase shift – the Gouy phase shift. The red solid curves in both graphs in Fig. 4 are fits calculated according to the procedure for processing the experimental data presented below. Fig. 4(c) once again displays the processed experimental points for the Gouy phase shown already in graph (b), now along with two additional dashed curves. They indicate the uncertainty of the processed data when the ±7.5 % uncertainty of the Rayleigh lengths due to the beam ellipticity is considered.

The solid magenta curve is a plot of the analytical formula for the Gouy phase shift for a Gaussian beam with a beam radius of 35 μm at the beam waist and for $\lambda = 532$ nm.

3.2. Data recording and processing

In the experimental setups shown in Fig. 3, the CCD camera is placed on a rail such that it can be translated along the beam axis (the z-axis in Figs. 4–8) in a well-defined way. In this manner, we are able to record interference patterns containing information on the Gouy phase vs. propagation distance. At each position, the CCD camera captures an interferogram. From each interferogram we evaluate the intensity in the center of the ring interference pattern, in the following referred to as axial interference signal. One such signal, is presented in Fig. 5(a). The sequence of operations for processing the experimental data is:

/a/ Subtraction of a reference line from the recorded axial interference signal in order to take into account the change of the beams' intensities;

/b/ Shift and normalization of the experimental data to fit them into the interval $[-1,1]$;

/c/ Approximation of the normalized interference signal with a function of the type

$$A + B\exp[-(z-C)^2/D]\sin\{2\pi[(z-E)/F + (z-G)^2/H + I]\},$$

where z is the longitudinal coordinate. The second term involving parameters B, C and D accounts for the longitudinal intensity variation of the interfering beams and A is a adjustable shift. Parameters E, F, G and H are related to the Gouy phase, while I is constant phase shift;

/d/ Apply $\arcsin\{\sin[\cdots]\}$ in order to transfer the obtained approximation of the experimental data to the range [-π, π];

/e/ Unfold the obtained approximation phase to a multiple of π.

/f/ Apply arcsin-function to the experimental data and repeat the procedure in the preceding point;

/g/ If desired for better visualization, shift the experimental data and the fit curve by the same phase. Present the propagation distance in physical units (e.g. in centimeters).

The sequence of graphs in Fig. 5 is visualizing the results of these operations applied to experimental data (Fig. 5(a)) obtained by imprinting and subsequently annihilating OVs with TCs 39 and −39. The resulting ring-shaped beam is focused with a lens of a focal length $f = 75$ cm. In this particular case the Mach-Zehnder interferometer is used. In the upper parts of Graphs (b) and (c) in Fig. 5, the sequences of the performed operations are indicated according to the explanations above. The data for the retrieved Gouy phase shift are denoted in Fig. 5(c) with open circles.

3.3. Results

Following the described procedure, we present a comparison between the experimental data and the theoretical results for different values of experimental parameters. One such parameter is the radius-to-width ratio r_0/ω_0 of the ring-shaped beam prior to its final focusing (here, a lens with $f = 75$ cm is used). In order to vary r_0/ω_0, we intentionally changed the TCs of the initially imprinted and subsequently annihilated OVs. The proportionality of r_0/ω_0 to the TC ℓ is in agreement with the data in Fig. 2(b) in [31]. (See also Table 1 below.) The data are obtained by using the Mach-Zehnder interferometer and refer to a relatively weak beam focusing. In Fig. 6(a)

Optics EXPRESS

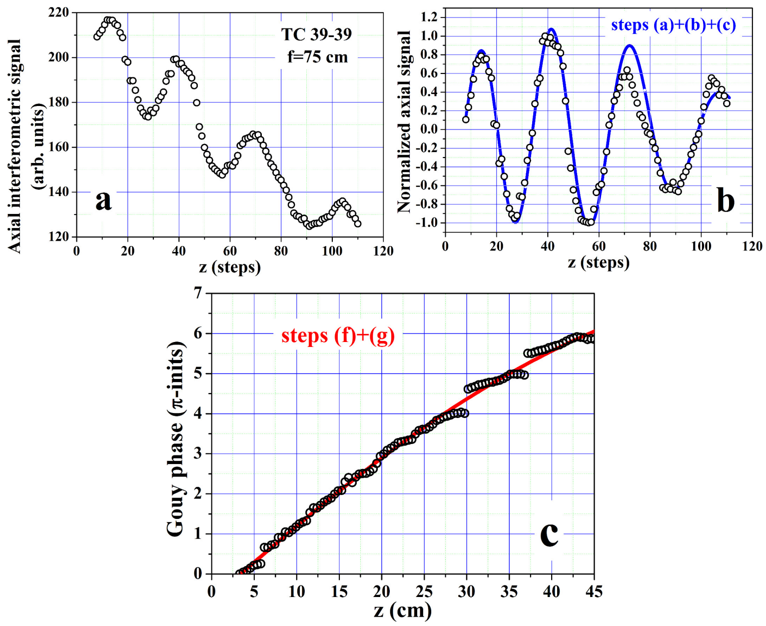

Fig. 5. Visualization of the sequence of operations that we followed in processing the experimental data in the case of initially imprinted and subsequently annihilated OVs with TCs 39 and −39, thereafter focusing the ring-shaped beam with a lens of a focal length $f = 75$ cm. Graph (a) – raw experimental data; Graph (b) – shift and normalized experimental data (open circles) and their analytical approximation (solid blue curve); Graph (c) – Gouy phase resulting from the unfolding procedure (presented in details in text) applied to the experimental points in graph (b), and fit curve.

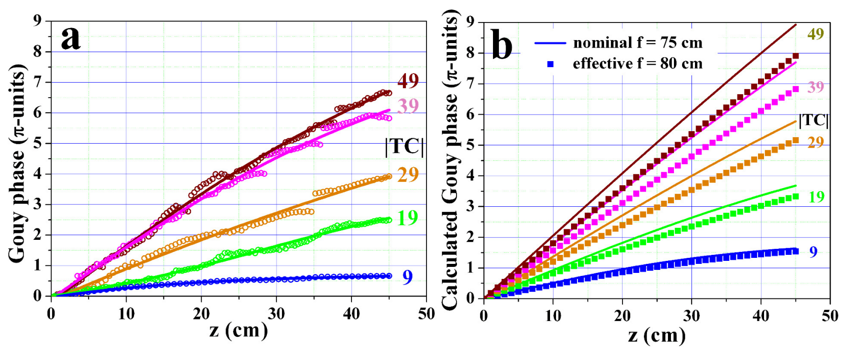

Fig. 6. (a): Longitudinal evolution of the Gouy phase of Bessel-Gaussian beams created by initially encoding and subsequently annihilating optical vortices with different topological charges. Their absolute values |TC| are indicated to the right of the curves. Experimental realization – Mach-Zehnder interferometer. Focal length of the lens $f = 75$ cm. (b): Longitudinal change of the Gouy phase calculated according Eq. (32) with parameters corresponding to the topological charges indicated to the right. Solid lines refer to nominal $f = 75$ cm, solid squares – to effective $f = 80$ cm. (See text for details.)

Optics EXPRESS

Table 1. Measured ring-shaped beam radius-to-width ratio r_0/ω_0, divergence half-angle and retrieved slope of the nearly linearly increasing Gouy phase vs. propagation length for Bessel-Gaussian beams generated by creating and annihilating OVs with different topological charges |TC|. Last row – retrieved slope of the Gouy phase of a Gaussian beam within the Rayleigh range. The retrieved data are accurate to the second decimal place.

|TC|	r_0/ω_0	Divergence half-angle (μrad)	Slope (f = 75 cm)
9	8.7	85	$0.01(4)\pi$/cm
19	13.5	67	$0.06(1)\pi$/cm
29	19.3	65	$0.09(1)\pi$/cm
39	26.5	49	$0.13(8)\pi$/cm
49	31.7	43	$0.15(4)\pi$/cm
Gaussian beam	—	—	$0.38(4)\pi$/cm (within the Rayleigh range)

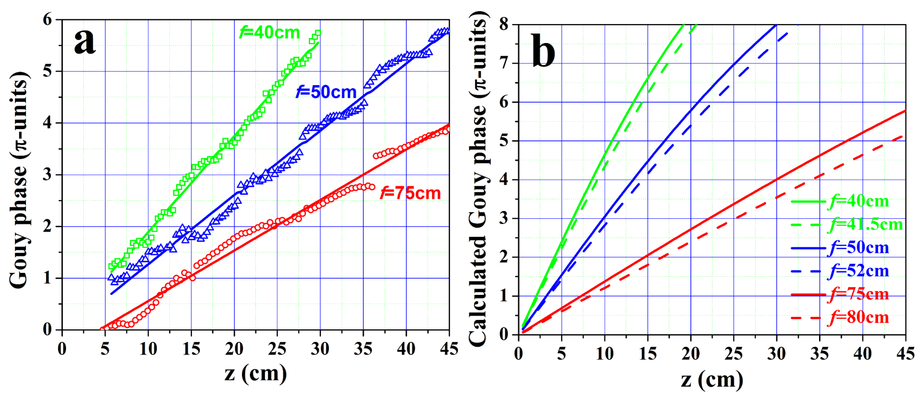

Fig. 7. Graph (a) – Longitudinal evolution of the Gouy phase of BGBs for |TC| = 29 and with lenses with nominal focal lengths f = 75 cm, 50 cm, and 40 cm. Open symbols – experimental points, solid lines – linear fits. Experimental realization – Mach-Zehnder interferometer. Graph (b) – Longitudinal evolution of the Gouy phase, calculated according Eq. (32) with parameters corresponding to |TC| = 29. Solid curves – results for the mentioned nominal focal lengths. Dashed curves – results for the experimentally measured effective focal lengths f = 80 cm, 52 cm, and 41.5 cm. See the text for details.

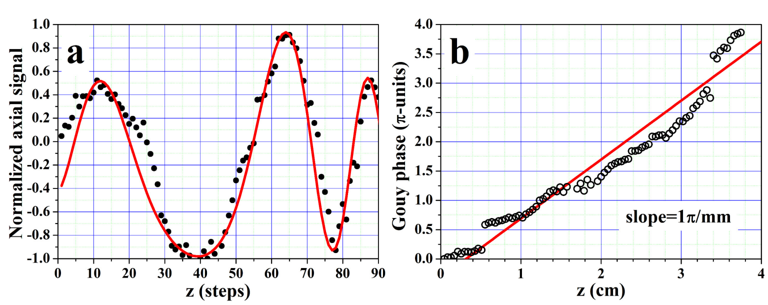

Fig. 8. Graph (a) – Shift and normalized experimental data (solid circles) and their approximation (solid red curve) with a function described in details in Section 3.2. Graph (b) – Processed experimental data (open circles) and their linear fit (red solid line). Experimental realization – single lens interferometer (see Fig. 3(b)).

Optics EXPRESS

we show processed experimental data (open circles) for the longitudinal evolution of the Gouy phase of Bessel-Gaussian beams created with TCs = 9, 19, 29, 39, and 49. The absolute values |TC| are indicated to the right of the curves. The solid lines are fits obtained as described above.

Two important tendencies are evident: (*i*) For all TCs, i.e. for every particular value of r_0/ω_0, the nearly linear dependence of Φ_G vs. z is well expressed. (*ii*) At a constant distance, the increase of the Gouy phase with increasing |TC| (i.e. the radius-to-width ratio r_0/ω_0) is in a qualitative agreement with the analytical result Eq. (32). This implies that the Gouy phase of the BGBs can be controlled without any realignment of the setup. However, for experiments where constant intensity is desired, one would need to adjust the pulse energy.

The theoretical results given by Eq. (32) are plotted in Fig. 6(b) with solid curves for the nominal focal length $f = 75$ cm of the used focusing lens. A Gaussian beam, however, does not focus exactly in the focal plane of a lens [46]. Because of this, it is important to know the $z = 0$ position of the focal plane of the lens. That is why we performed a calibration experiment. We concluded that the effective focal length of the used lens with nominal $f = 75$ cm is 80 cm. The evolution of the Gouy phase for the nominal and experimentally determined (effective) focal lengths, computed using Eq. (32), are compared in Fig. 6(b). As seen, the longer effective focal length results in a decrease in the Gouy phase at a fixed distance.

The comparison between the experimental (Fig. 6(a)) and theoretical data (Fig. 6(b)) for the nominal $f = 75$ cm at e.g. 40 cm for |TC| = 49 shows that the calculated Gouy phase is nearly 20% higher than the experimentally measured. However, this 20% higher theoretical value decreases nearly three times to approximately 7% when taking into the account the effective focal length of the used lens ($f = 80$ cm). In our view, this difference is due to the sensitivity of the Gouy phase to the accuracy in determining the ring width ω_0 of the ring-shaped beam prior to Fourier transformation. Additional comments regarding the origin of this error can be found in Supplement 1.

In Table 1, we summarize the experimental results for the retrieved slopes of the respective Gouy phases of the BGBs for different radius-to-width ratios. In addition, the divergence half-angles of the central peaks of the BGBs are presented. As expected (see e.g. [31]), the increase of the radius-to-width ratio r_0/ω_0 of the ring-shaped beam in front of the lens leads to a decrease of the beam's divergence. For the slope of the Gouy phase vs. |TC| the tendency is the opposite. It increases from 0.01π/cm at |TC| = 9 to 0.15π/cm at |TC| = 49. These slopes for the Gouy phase of BGBs referring to a relatively weak focusing are still lower than the 0.38π/cm for a Gaussian beam, however the last value is estimated within its Rayleigh range (within few centimeters), while the Gouy phase of BGBs increases nearly linearly over tens of centimeters.

Another accessible experimental control parameter is the focal length of the Fourier-transforming lens L1. The data presented in Fig. 7 clearly show that the stronger the focusing of the ring-shaped beam, the higher the slope of the Gouy phase vs. propagation distance. In Fig. 7(a) we show experimental results for this dependence for BGBs generated by imprinting and annihilating TCs = 29 and −29. Three lenses with nominal focal lengths $f = 75$ cm, 50 cm, and 40 cm are used. The Gouy phases calculated using Eq. (32) are shown in Fig. 7(b). The solid curves refer to the denoted and already mentioned nominal focal lengths, the dashed curves to the somewhat longer experimentally determined effective focal lengths of 80 cm, 52 cm, and 41.5 cm. For one and the same propagation distance, stronger focusing causes a larger Gouy phase shift of the BGB. The calculated phase shift surpass the measured, however the differences decrease when the effective focal lengths are accounted in the calculations instead of the nominal ones. For shorter focal lengths, the calculated Gouy phase deviates more strongly (almost by a factor of 2) from the experimental results. We attribute this discrepancy to the sensitivity of the Gouy phase to the accuracy in determining the ring width ω_0 of the ring-shaped beam prior to Fourier transformation. More details can be found in Supplement 1.

Optics EXPRESS

Additionally, analogous to the classical f-number, we can define an effective f-number as a ratio of the lens' focal length f to the ring radius r_0. As seen from Eq. (32), the Gouy phase depends inversely proportional to the second power of this effective f-number.

We would like to show experimental data for stronger focusing (but still moderate, as compared to focusing with e.g. high numerical aperture objective [39]). This is realized by using the single-lens interferometer technique described in details in [44] and shown in Fig. 3(b). Obviously, the propagation length for the "ghost" BGB is limited, since after its focus it converts into a diverging ring-shaped beam. The host BGB (more precisely – its central peak) effectively serves as a reference beam. Within the distance of interest, the weakly focused host BGB is only slightly reshaped. Ascribing the longitudinal phase changes solely to the more strongly focused "ghost" BGB, the normalized axial signal and the data retrieved from this measurement are shown in Fig. 8(a) and (b), respectively. They clearly express the fact that a slope of the Gouy phase vs. distance of 1.0π/mm is achievable under moderate focusing (estimated focal length 14.6 cm). The reconstructed change of the Gouy phase here is almost 4π (see Fig. 8(b)), while the Gouy phase of the Gaussian beam should saturate at larger offsets from its beam waist and should remain limited to $\pm\pi/2$.

4. Conclusion

The problem of the Gouy phase of Bessel-Gaussian beams (BGBs) still raises many questions. Its correct determination is of a great importance for many fields of modern optics. Here, we elaborated an analytical model for the Gouy phase of long-range BGBs obtained by creating and annihilating optical vortices (OVs). The model is accounting for the influence of the relevant experimental parameters: the OV's topological charge, the ring-shaped beam's radius-to-width ratio, and the focal length of the Fourier-transforming lens. These parameters are relevant because their combination determines the transverse component of the wave-vector. The experimental data support the model and prove the nearly linear evolution of the Gouy phase of BGBs both for long and short focal lengths. In particular, for the same ring-shaped beam and propagation distance, stronger focusing causes a larger Gouy phase shift of the BGB. Under relatively weak focusing of the initial hollow ring-shaped beam, the Gouy phase of the BGB is found to change linearly at a rate of some $0.2\,\pi$/cm over a distance of 45 cm. Under moderate focusing, the linear Gouy phase vs. propagation distance reaches a slope of $1.0\,\pi$/mm over distances exceeding 4 mm. The presented results are important in e.g., nonlinear optics in optically thick nonlinear media, where the observation of nonlinear processes requires high peak intensities and phase matching of focused beams. They may appear applicable also to filaments formation and high-harmonics generation.

Funding. Ministry of Education and Science (D01-401/18.12.2020); Deutsche Forschungsgemeinschaft (PA 730/13).

Acknowledgements. We acknowledge funding of the Deutsche Forschungsgemeinschaft (project PA PA730/13). This work was also supported by the European Regional Development Fund within the Operational Programme "Science and Education for Smart Growth 2014-2020" under the Project CoE "National center of mechatronics and clean technologies" BG05M2OP001-1.001-0008-C01 and by the Bulgarian Ministry of Education and Science as a part of National Roadmap for Research Infrastructure, grant number D01-401/18.12.2020 (ELI ERIC BG). L.S. would like to gratefully acknowledge the research scholarship granted by the Alexander von Humboldt Foundation.

Disclosures. The authors declare no conflicts of interest.

Data Availability. The datasets generated and analyzed during the current study are available from the corresponding author upon a reasonable request.

Supplemental document. See Supplement 1 for supporting content.

References

1. E. H. Linfoot and E. Wolf, "Phase distribution near focus in an aberration-free diffraction image," Proc. Phys. Soc., London, Sect. B **69**(8), 823–832 (1956).

Optics EXPRESS

2. G. W. Farnell, "Phase distribution in the focal region of a microwave lens system," Ph.D. thesis, Eaton Electronics Research Laboratory, McGill University (2012).
3. G. W. Farnell, "Measured phase distribution in the image space of a microwave lens," Can. J. Phys. **36**(7), 935–943 (1958).
4. W. H. Carter, "Anomalies in the field of a Gaussian beam near focus," Opt. Commun. **7**(3), 211–218 (1973).
5. Y. Toda, S. Honda, and R. Morita, "Dynamics of a paired optical vortex generated by second-harmonic generation," Opt. Express **18**(17), 17796–17804 (2010).
6. X. Wang, W. Sun, Y. Cui, J. Ye, S. Feng, and Y. Zhang, "Complete presentation of the Gouy phase shift with the THz digital holography," Opt. Express **21**(2), 2337–2346 (2013).
7. S. Ahmed, J. Savolainen, and P. Hamm, "The effect of the Gouy phase in optical-pump-THz-probe spectroscopy," Opt. Express **22**(4), 4256–4266 (2014).
8. M. Liebmann, A. Treffer, M. Bock, T. Elsaesser, and R. Grunwald, "Spectral anomalies and Gouy rotation around the singularity of ultrashort vortex pulses," Opt. Express **25**(21), 26076–26088 (2017).
9. S. M. Baumann, D. M. Kalb, L. H. MacMillan, and E. J. Galvez, "Propagation dynamics of optical vortices due to Gouy phase," Opt. Express **17**(12), 9818–9827 (2009).
10. X. Pang and T. D. Visser, "Manifestation of the Gouy phase in strongly focused, radially polarized beams," Opt. Express **21**(7), 8331–8341 (2013).
11. Y. Zhang, X. Guo, L. Han, P. Li, S. Liu, H. Cheng, and J. Zhao, "Gouy phase induced polarization transition of focused vector vortex beams," Opt. Express **25**(21), 25725–25733 (2017).
12. M. M. Sánchez-López, J. A. Davis, I. Moreno, A. Cofré, and D. M. Cottrell, "Gouy phase effects on propagation of pure and hybrid vector beams," Opt. Express **27**(3), 2374–2386 (2019).
13. R. W. Boyd, *Nonlinear Optics (Third Edition)* (Academic, 2008).
14. N. Lastzka and R. Schnabel, "The Gouy phase shift in nonlinear interactions of waves," Opt. Express **15**(12), 7211–7217 (2007).
15. R. F. Offer, A. Daffurn, E. Riis, P. F. Griffin, A. S. Arnold, and S. Franke-Arnold, "Gouy phase-matched angular and radial mode conversion in four-wave mixing," Phys. Rev. A **103**(2), L021502 (2021).
16. F. Lindner, G. G. Paulus, H. Walther, A. Baltuška, E. Goulielmakis, M. Lezius, and F. Krausz, "Gouy phase shift for few-cycle laser pulses," Phys. Rev. Lett. **92**(11), 113001 (2004).
17. B. Ghomashi, R. Reiff, and A. Becker, "Coherence in macroscopic high harmonic generation for spatial focal phase distributions of monochromatic and broadband Gaussian laser pulses," Opt. Express **29**(24), 40146–40160 (2021).
18. S. Feng and H. G. Winful, "Physical origin of the Gouy phase shift," Opt. Lett. **26**(8), 485–487 (2001).
19. J. Hamazaki, Y. Mineta, K. Oka, and R. Morita, "Direct observation of Gouy phase shift in a propagating optical vortex," Opt. Express **14**(18), 8382–8392 (2006).
20. J. He, X. Wang, D. Hu, J. Ye, S. Feng, Q. Kan, and Y. Zhang, "Generation and evolution of the terahertz vortex beam," Opt. Express **21**(17), 20230–20239 (2013).
21. F. Schlaepfer, A. Ludwig, M. Lucchini, L. Kasmi, M. Volkov, L. Gallmann, and U. Keller, "Gouy phase shift for annular beam profiles in attosecond experiments," Opt. Express **25**(4), 3646–3655 (2017).
22. S. N. Khonina, A. V. Ustinov, and S. Chávez-Cerda, "Generalized parabolic nondiffracting beams of two orders," J. Opt. Soc. Am. A **35**(9), 1511–1517 (2018).
23. J. Durnin, J. J. Miceli, and J. H. Eberly, "Diffraction-free beams," Phys. Rev. Lett. **58**(15), 1499–1501 (1987).
24. G. Indebetouw, "Nondiffracting optical fields: some remarks on their analysis and synthesis," J. Opt. Soc. Am. A **6**(1), 150–152 (1989).
25. P. Martelli, M. Tacca, A. Gatto, G. Moneta, and M. Martinelli, "Gouy phase shift in nondiffracting Bessel beams," Opt. Express **18**(7), 7108–7120 (2010).
26. D. McGloin and K. Dholakia, "Bessel beams: Diffraction in a new light," Contemp. Phys. **46**(1), 15–28 (2005).
27. C. Vetter, R. Steinkopf, K. Bergner, M. Ornigotti, S. Nolte, H. Gross, and A. Szameit, "Realization of free-space long-distance self-healing Bessel beams," Laser Photonics Rev. **13**(10), 1900103 (2019).
28. X. Yu, A. Todi, and H. Tang, "Bessel beam generation using a segmented deformable mirror," Appl. Opt. **57**(16), 4677–4682 (2018).
29. R. Bowman, N. Muller, X. Zambrana-Puyalto, O. Jedrkiewicz, P. D. Trapani, and M. J. Padgett, "Efficient generation of Bessel beam arrays by means of an SLM," Eur. Phys. J. Spec. Top. **199**(1), 159–166 (2011).
30. M. Duocastella and C. Arnold, "Bessel and annular beams for materials processing," Laser Photonics Rev. **6**(5), 607–621 (2012).
31. L. Stoyanov, M. Zhekova, A. Stefanov, I. Stefanov, G. G. Paulus, and A. Dreischuh, "Zeroth- and first-order long range non-diffracting Gauss–Bessel beams generated by annihilating multiple-charged optical vortices," Sci. Rep. **10**(1), 21981 (2020).
32. L. Stoyanov, M. Zhekova, A. Stefanov, B. Ivanov, I. Stefanov, G. G. Paulus, and A. Dreischuh, "Generation of long range low-divergent Gauss–Bessel beams by annihilating optical vortices," Opt. Commun. **480**, 126510 (2021).
33. L. Stoyanov, Y. Zhang, A. Dreischuh, and G. G. Paulus, "Long-range quasi-non-diffracting Gauss-Bessel beams in a few-cycle laser field," Opt. Express **29**(7), 10997–11008 (2021).
34. J. E. Shrock, B. Miao, L. Feder, and H. M. Milchberg, "Meter-scale plasma waveguides for multi-GeV laser wakefield acceleration," Phys. Plasmas **29**(7), 073101 (2022).

Optics EXPRESS

35. M. Davino, A. Summers, T. Saule, J. Tross, E. McManus, B. Davis, and C. Trallero-Herrero, "Higher-order harmonic generation and strong field ionization with Bessel–Gauss beams in a thin jet geometry," J. Opt. Soc. Am. B **38**(7), 2194–2200 (2021).
36. P. Polesana, M. Franco, A. Couairon, D. Faccio, and P. Di Trapani, "Filamentation in Kerr media from pulsed Bessel beams," Phys. Rev. A **77**(4), 043814 (2008).
37. A. Averchi, D. Faccio, R. Berlasso, M. Kolesik, J. V. Moloney, A. Couairon, and P. Di Trapani, "Phase matching with pulsed Bessel beams for high-order harmonic generation," Phys. Rev. A **77**(2), 021802 (2008).
38. L. Van Dao, K. B. Dinh, and P. Hannaford, "Generation of extreme ultraviolet radiation with a Bessel–Gaussian beam," Appl. Phys. Lett. **95**(13), 131114 (2009).
39. M.-S. Kim, T. Scharf, A. da Costa Assafrao, C. Rockstuhl, S. F. Pereira, H. P. Urbach, and H. P. Herzig, "Phase anomalies in Bessel-Gauss beams," Opt. Express **20**(27), 28929–28940 (2012).
40. G. Vampa, T. J. Hammond, N. Thiré, B. E. Schmidt, F. Légaré, C. R. McDonald, T. Brabec, and P. B. Corkum, "Linking high harmonics from gases and solids," Nature **522**(7557), 462–464 (2015).
41. J. W. Goodman, *Introduction to Fourier Optics* (Roberts and Company Publishers, 2005).
42. I. Gradshteyn and I. Ryzhik, *Table of Integrals, Series, and Products (Seventh Edition)* (Academic, 2007).
43. F. Gori, G. Guattari, and C. Padovani, "Bessel-Gauss beams," Opt. Commun. **64**(6), 491–495 (1987).
44. J. Peatross and M. V. Pack, "Visual introduction to Gaussian beams using a single lens as an interferometer," Am. J. Phys. **69**(11), 1169–1172 (2001).
45. P. Munjal and K. P. Singh, "A single-lens universal interferometer: Towards a class of frugal optical devices," Appl. Phys. Lett. **115**(11), 111102 (2019).
46. F. L. Perdotti, L. M. Perdotti, and L. S. Perdotti, *Introduction to Optics* (Cambridge University, 2017).